Journal of Materials Chemistry A

ROYAL SOCIETY OF CHEMISTRY

PAPER

Cite this: *J. Mater. Chem. A*, 2021, **9**, 12299

$NiCo_2O_4$ nanosheets as a novel oxygen-evolution-reaction cocatalyst *in situ* bonded on the g-C_3N_4 photocatalyst for excellent overall water splitting†

Cheng Cheng,‡ Liuhao Mao,‡ Jinwen Shi,* Fei Xue, Shichao Zong, Botong Zheng and Liejin Guo

Received 9th January 2021
Accepted 29th April 2021

DOI: 10.1039/d1ta00241d

rsc.li/materials-a

A 2D/2D coupled $NiCo_2O_4$/g-C_3N_4 nanostructure was fabricated through an *in situ* growth strategy. $NiCo_2O_4$ worked as a novel oxygen-evolution-reaction cocatalyst, and the intimate interface combination by surface bonding and the related cooperative effect between $NiCo_2O_4$ and g-C_3N_4 were comprehensively explored. Consequently, the separation and migration of photo-generated charge carriers for g-C_3N_4 were efficiently promoted, as well as the energy barriers of the oxygen evolution reaction were reduced. $NiCo_2O_4$/g-C_3N_4 showed obviously enhanced photocatalytic O_2-evolution activity (4.6 times that of bare g-C_3N_4), and the corresponding AQY achieved 4.9% at 380 nm. Then, Pt as a hydrogen-evolution-reaction cocatalyst was employed to cooperate with $NiCo_2O_4$ to construct dual cocatalyst loaded g-C_3N_4 for photocatalytic overall water splitting, in which H_2 and O_2 simultaneously evolved in a stoichiometric ratio of 2 : 1, and the AQY for H_2 evolution reached 2.8% at 380 nm. Consequently, this work demonstrates a reliable strategy for g-C_3N_4 to construct a photocatalytic system for efficient overall water splitting.

1. Introduction

Hydrogen evolution based on photocatalytic water splitting technology is regarded as a prospective approach to transform solar energy into available, clean and transportable chemical energy, for alleviating the excessive demand for fossil energy as well as improving the correlative environmental problem.[1–3] As for photocatalytic overall water splitting, remarkable advances have been witnessed by far in the exploitation of water reduction reaction which for instance can be markedly promoted by Pt-cocatalysts,[4–7] whereas the half reaction of water oxidation to oxygen usually suffers limited activity due to its complicated four-electron oxidation reaction and large thermodynamic activation energy barrier for the formation of oxygen molecules.[8–10] Thus, photocatalytic O_2 evolution reaction (OER) is the crucial performance-limiting step and remains the main challenge for achieving high efficiency of photocatalytic overall water splitting.

For many photocatalysts with poor OER activity, their immanent limits could be explored using a good model case of water electrolysis: these semiconductor-based catalysts commonly possess poor electrocatalytic activities and require large overpotentials for driving chemical transformations.[11,12] As a result, implanting suitable electrocatalysts as cocatalysts into photocatalysts to construct hybrid systems is proposed as an effective strategy which can dramatically improve photocatalytic activity.[13–15] On the one hand, benefiting from lower activation energy, cocatalysts act as surface active sites where chemical transformations could be thermodynamically favorable as compared to those directly on semiconductor-based photocatalysts. On the other hand, loading cocatalysts on semiconductor-based photocatalysts can also inhibit the charge recombination and reverse reaction. Recently, many electrocatalysts have been used as reduction cocatalysts and assembled with photocatalysts for the H_2 evolution reaction (HER), such as Ni_2P, CoP, FeP, Cu_3P, MoP and NiCoP.[16–22] However, only a few reports focused on the applications of OER electrocatalysts as oxidation cocatalysts for photocatalytic O_2 evolution, and most of them lack interface/junction design between the photocatalyst and cocatalyst.[23] $NiCo_2O_4$ has been reported as an efficient noble-metal-free electrocatalyst for the OER in which it delivers a low overpotential.[24,25] Thus $NiCo_2O_4$ is a promising candidate for OER cocatalysts, and yet the $NiCo_2O_4$-containing photocatalytic system for O_2 production or overall water splitting has rarely received prior investigations.

Among the various host photocatalysts, polymeric graphitic carbon nitride (g-C_3N_4) with a 2D conjugated structure emerges as a shining star in the field of photocatalysis, because of its important merits of environmental friendliness, earth-

International Research Center for Renewable Energy (IRCRE), State Key Laboratory of Multiphase Flow in Power Engineering (MFPE), Xi'an Jiaotong University, Xi'an 710049, China. E-mail: jinwen_shi@mail.xjtu.edu.cn

† Electronic supplementary information (ESI) available. See DOI: 10.1039/d1ta00241d

‡ These authors contributed equally to this work.

abundant nature, specific planar structure, good stability, and appropriate thermodynamical potentials for H_2 and O_2 evolution reactions.[26–28] Nevertheless, the rapid recombination of photo-induced charge carriers as well as the especially poor photocatalytic OER activity of bare g-C_3N_4 result in low efficiency of photocatalytic overall water splitting, thus limiting its industrial applications.[29,30] Coupling with a suitable OER cocatalyst can simultaneously settle the above drawbacks, and g-C_3N_4 can be regarded as an excellent host to support suitable cocatalysts to construct enhanced photocatalytic overall water splitting systems through tailor design of the coupled structure between g-C_3N_4 and the cocatalyst.

Herein, $NiCo_2O_4$ nanosheets were *in situ* grown on the surface of g-C_3N_4 to fabricate a 2D/2D coupled structure. The intimate interface combination between $NiCo_2O_4$ nanosheets and g-C_3N_4, as well as the cocatalytic effect of $NiCo_2O_4$ was carefully characterized and analyzed. In addition, Pt was employed as a HER cocatalyst and cooperated with the $NiCo_2O_4$/g-C_3N_4 coupled structure to perform photocatalytic overall water splitting, and this demonstrates a reliable strategy for g-C_3N_4 to construct photocatalytic overall water splitting systems *via* assistance by dual reduction and oxidation cocatalysts.

2. Experimental section

2.1 Preparation of photocatalysts

2.1.1 Preparation of g-C_3N_4. The g-C_3N_4 photocatalyst was prepared according to previous work.[31] Urea (10 g) was calcined at 600 °C for 4 h under air atmosphere with a ramping rate of 15 °C min^{-1} in an alumina crucible with a cover. After cooling down to room temperature, the g-C_3N_4 photocatalyst (denoted as CN) was obtained.

2.1.2 Preparation of $NiCo_2O_4$/g-C_3N_4, $NiCo_2O_4$, NiO_x/g-C_3N_4 and CoO_x/g-C_3N_4. In a typical procedure, CN (100 mg) and certain amounts of $CoCl_2 \cdot 6H_2O$, $NiCl_2 \cdot 6H_2O$ (the molar ratio was 2 : 1) were added into water (250 mL) followed by sonication for 2 h to obtain a homogeneous dispersion, and then hexamethylenetetramine (HMT) (8.75 mmol) was dissolved into the dispersion. Subsequently, the dispersion was transferred into a round-bottomed flask (500 mL) and refluxed at 100 °C in an oil bath for 5 h with continuous stirring. After washing 3 times with water, the product was collected by centrifugation and dried at 50 °C. The obtained powder was then calcined at 400 °C for 2 h in air to get the $NiCo_2O_4$/g-C_3N_4 coupled hybrid (denoted as CN-*x*NiCoO), in which *x*% ($x = 0.00$, 0.25, 0.50, 1.00, 1.50 and 2.00) meant the mass ratio of the Co element to CN. Bare $NiCo_2O_4$ was prepared under the same conditions in the absence of CN, and with the amounts of 1.8750 and 0.9375 mmol (the molar ratio was 2 : 1) for $CoCl_2 \cdot 6H_2O$ and $NiCl_2 \cdot 6H_2O$, respectively. The intermediate without calcination in air was denoted as NiCoO-pre and the bare $NiCo_2O_4$ was denoted as NiCoO. NiO_x/g-C_3N_4 (denoted as CN-1.50NiO_x) and CoO_x/g-C_3N_4 (denoted as CN-1.50CoO_x) were also prepared under the same conditions except that $CoCl_2 \cdot 6H_2O$ or $NiCl_2 \cdot 6H_2O$ was not added, respectively, and the mass ratio was controlled at 1.50 wt% for the Ni or Co element to CN.

2.1.3 Preparation of (Pt, $NiCo_2O_4$)/g-C_3N_4, (Pt, NiO_x)/g-C_3N_4, (Pt, CoO_x)/g-C_3N_4 and Pt/g-C_3N_4. CN-1.00NiCoO, CN-1.50NiO_x or CN-1.50CoO_x (80 mg) was added into water (80 mL) to form a homogeneous dispersion. Pt (2.4 mg, corresponding to 3% of the mass of photocatalyst) as a HER cocatalyst was loaded on the above sample *via* the typical *in situ* photodeposition strategy from the precursor of $H_2PtCl_6 \cdot 6H_2O$. Before photodeposition reaction, the reactor was purged with Ar for 30 min to eliminate O_2. After 2 h reaction, the corresponding product was collected by thoroughly washing with water and dried in a vacuum oven for 12 h at 60 °C, and was denoted as 3Pt-CN-1.00NiCoO, 3Pt-CN-1.50NiO_x or 3Pt-CN-1.50CoO_x. Pt/g-C_3N_4 was prepared using a similar photodeposition procedure except that triethanolamine (TEOA 10 vol%) as a hole sacrificial agent was used in the reaction solution, and the final product was denoted as CN-3Pt.

2.2 Photocatalytic measurements

Photocatalytic water splitting reactions were performed in a Pyrex glass reactor (110 mL) in which light was irradiated from the side window. A Xe lamp (300 W) as the light source provided full-arc or visible-light irradiation (with a 400 nm cut-off filter). The light spectra before and after the filter are shown in Fig. S1.† For the photocatalytic O_2 evolution reaction, the photocatalyst (50 mg), La_2O_3 (160 mg) and $AgNO_3$ (136 mg) were sequentially dispersed in an aqueous solution (80 mL) with stirring, in which $AgNO_3$ and La_2O_3 were used as the electron acceptor and pH buffer agent, respectively. For the photocatalytic overall water splitting reaction, it was performed in the same system, and the photocatalyst (50 mg) was dispersed in deionized water (80 mL) with stirring. Before the photocatalytic reaction, the reactor was purged with Ar for 30 min to eliminate O_2. The evolved gas was detected using a North Point NP-GC-901A gas chromatograph (Ar as carrier gas, thermal conductivity detector (TCD), TDX-01 column) per 1 h, and a syringe gas sampling technique was used. The gas sampling data are shown in Fig. S2a and b.† The details of the measurement of apparent quantum yield (AQY) are presented in the ESI,† and the UV-vis spectra of different band-pass filters of 380, 405, 425, 440 and 480 nm are shown in Fig. S2c–g.†

3. Results and discussion

3.1 Composition and structure

The overall strategy for *in situ* growth and assembly of $NiCo_2O_4$ nanosheets on g-C_3N_4 is illustrated in Fig. 1. Co^{2+} and Ni^{2+} ions were first adhered to the surface of g-C_3N_4 in the forms of hydroxides, and then a calcination procedure was implemented to make $NiCo_2O_4$ nanosheets *in situ* grow on g-C_3N_4 for obtaining the $NiCo_2O_4$/g-C_3N_4 coupled composite (see details in Fig. S3, S4, S6–S8†). In Fig. S4a and b,† we see the XRD patterns of NiCoO whose diffraction peaks correspond to cubic-phase $NiCo_2O_4$ (JCPDS no. 020-0781), verifying the successful preparation of $NiCo_2O_4$. As for CN-*x*NiCoO ($x = 0.00$, 0.25, 0.50, 1.00, 1.50 and 2.00), typical (100) and (002) diffraction peaks were observed for all the samples, respectively, which were indexed to

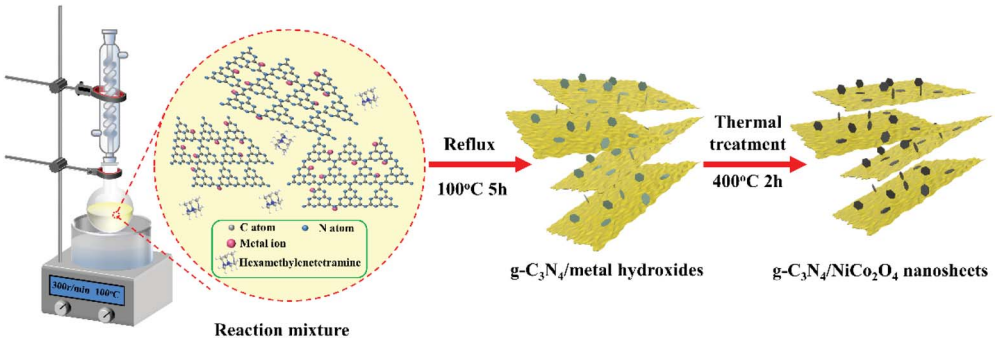

Fig. 1 Fabrication procedure of $NiCo_2O_4$ *in situ* grown on g-C_3N_4.

the typical characteristics of g-C_3N_4.[31–33] Structurally, the former minor angle diffraction peak was attributed to the in-plane arrangement of tri-*s*-triazine units, and another strong diffraction peak corresponded to the periodic inter-layer stacking of conjugated aromatic segments[34,35] It is noteworthy that the unchanged diffraction peak position indicated that the crystal structure of CN was little influenced by the integration of NiCoO. In addition, diffraction peaks indexed to cubic-phase $NiCo_2O_4$ could be observed in CN-2.00NiCoO but almost not in CN-*x*NiCoO (x = 0.00, 0.25, 0.50, 1.00 and 1.50) composites, which might be ascribed to their less dosage. For the control samples, CN-1.50NiO_x and CN-1.50CoO_x also showed typical characteristics of g-C_3N_4 (Fig. S4c†), and CN-0.00NiCoO and CN had almost the same XRD characteristics (Fig. S4d†). Fig. S5† gives the FTIR spectra of CN-0.00NiCoO, CN-1.00NiCoO, CN-1.50NiO_x and CN-1.50CoO_x. All the samples demonstrated the dominant features of the g-C_3N_4 structure, *i.e.*, the broad bands in the wavelength range of 2900–3340 cm^{-1} were indexed to the stretching vibrational absorptions of N–H, the peaks located at 1200–1700 cm^{-1} were assigned to the stretching vibration modes of aromatic tri-*s*-triazine repeating units, including sp^2 C=N stretching vibrations and sp^3 C–N out-of-plane bending vibrations, and the characteristic peak centered at 810 cm^{-1} was assigned to the out-of-plane breathing vibrations of tri-*s*-triazine units.[36–38]

Considering that the structure of NiCoO was not obviously observed in CN-1.00NiCoO duo to the low content (Fig. S3 and S6†), other samples with higher contents of NiCoO-pre and NiCoO were prepared and denoted as CN-10.00NiCoO-pre and CN-10.00NiCoO (Fig. S7†). It could be obviously observed that the nanosheet structure of NiCoO was intimately anchored on CN (Fig. S8†). As for the micro-nano structure of as-prepared CN-*x*NiCoO, by taking CN-1.00NiCoO as a typical example, TEM images showed that scattered NiCoO nanosheets decorated the CN nanosheet structure (Fig. 2a and b), and obvious lattice fringes (interplanar spacing of 0.203 nm) were observed and corresponded to the (400) plane of NiCoO (Fig. 2c).[24] Note that the NiCoO nanosheets on CN nanosheets had sizes less than ten nanometers in diameter, which was dramatically smaller than that of bare NiCoO, and besides that, the CN nanosheets existed as the substrate exerting a supporting effect, this difference could be attributed to the fact that in the preparation process of CN-*x*NiCoO, smaller amounts of $NiCl_2 \cdot 6H_2O$ and $CoCl_2 \cdot 6H_2O$ were added. Moreover, the coupled nanostructure of the $NiCo_2O_4$/g-C_3N_4 composite could be further investigated using the STEM image (Fig. 2d) and corresponding EDX elemental mapping results (Fig. 2e–i). Similar elemental distributions for C and N reflected the CN structure, while similar elemental distributions of Ni, Co and O clearly demonstrated the formation of NiCoO. In addition, obvious deviations and scattered distributions in elemental scopes demonstrated that NiCoO nanosheets were dispersedly assembled on the surface of CN nanosheets. These results directly proved the successful preparation of the 2D/2D $NiCo_2O_4$/g-C_3N_4 coupled structure and distinctly showed the intimate interfacial combination between NiCoO and CN supports.

3.2 Chemical states

The surface chemical states of CN-*x*NiCoO hybrids were next analyzed using XPS results. Firstly, by taking CN-0.00NiCoO and CN-1.00NiCoO as typical examples, Fig. 3a presents their survey-scan XPS spectra. Besides O, N, and C elements, Ni and Co signals appeared for CN-1.00NiCoO as compared to CN-0.00NiCoO. For the C 1s spectra (Fig. 3b), both samples showed three characteristic peaks with similar binding energies, for CN-1.00NiCoO, the peaks were ascribed to typical adventitious graphitic C species (C=C), sp^2 hybridized C bonded to –NH_x, and sp^2 C connected to N in N=C–N,

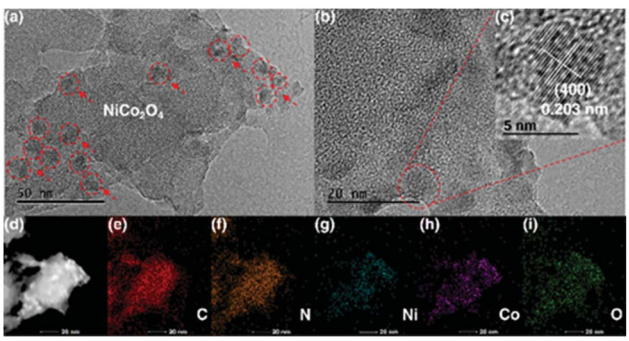

Fig. 2 (a) TEM image, (b and c) HRTEM images, (d) STEM image, and (e–i) EDX elemental mapping results of (e) C, (f) N, (g) Ni, (h) Co and (i) O for CN-1.00NiCoO.

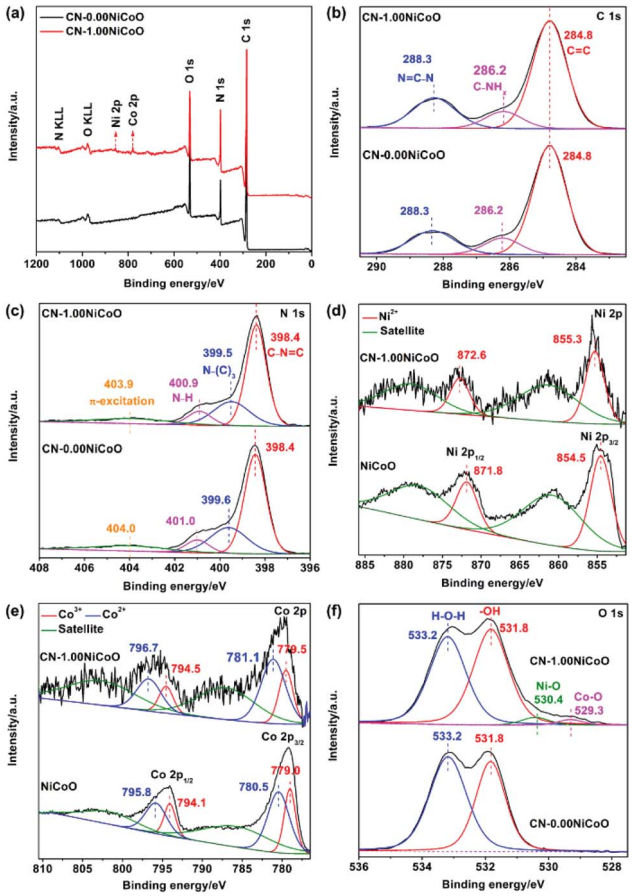

Fig. 3 (a) Survey-scan and high-resolution XPS spectra of (b) C 1s and (c) N 1s for CN-0.00NiCoO and CN-1.00NiCoO; (d and e) high-resolution XPS spectra of (d) Ni 2p and (e) Co 2p for CN-1.00NiCoO and NiCoO; (f) high-resolution XPS spectra of O 1s for CN-0.00NiCoO and CN-1.00NiCoO.

respectively.[39–41] The N 1s spectra of both samples could be divided into four peaks (Fig. 3c), for CN-1.00NiCoO, the peaks were assigned to sp^2 N in tri-*s*-triazine (C–N=C), bridging tertiary N in N–$(C)_3$, N in the heterocycle and N–H, and π-excitations, respectively.[39–41] In contrast, there were significant shifts towards lower binding energies of the N 1s peaks for CN-1.00NiCoO except the sp^2 N in C–N=C as compared to those of CN-0.00NiCoO. Secondly, comparison of the Ni 2p and Co 2p spectra between CN-1.00NiCoO and NiCoO was also made (Fig. 3d and e). The valence states of Ni and Co in CN-1.00NiCoO kept unchanged as compared to NiCoO, for CN-1.00NiCoO, the peaks centered at 872.6 and 855.3 eV were assigned to $2p_{1/2}$ and $2p_{3/2}$ of Ni^{2+}, the peaks centered at 794.5 and 779.5 eV were assigned to $2p_{1/2}$ and $2p_{3/2}$ of Co^{3+}, and the peaks centered at 796.7 and 781.1 eV were indexed to $2p_{1/2}$ and $2p_{3/2}$ of Co^{2+}.[24,42] Significantly, as compared to those of NiCoO, the characteristic peaks of Ni^{2+}, Co^{2+} and Co^{3+} for CN-1.00NiCoO all shifted towards higher binding energies. It is widely acknowledged that the unoccupied d orbitals of metal atoms could connect with the lone pair electrons from sp^3-hybridized N atoms to form metal–N bonds.[43–46] The above results indicated that new surface bonding states were built by coupling NiCoO with CN, and Co(δ^+) and Ni(δ^+) atoms were coupled with N atoms of tertiary nitrogen to build Co(δ^+)–N(δ^-) and Ni(δ^+)–N(δ^-) bonding states, resulting in decreased electron densities in metal atoms accompanied by increased electron densities in N atoms, which were consistent with the negative shifts of the binding energies for N 1s, as well as the positive shifts of the binding energies for Ni 2p and Co 2p in CN-1.00NiCoO.[43–46] In Fig. 3f, besides the characteristic peaks of H–O–H and –OH,[47] another two peaks assigned to Co–O and Ni–O were observed for CN-1.00NiCoO as compared to CN-0.00NiCoO. The results further confirmed the coupling structure of NiCoO and CN. In addition, CN-1.50NiO_x and CN-1.50CoO_x were also characterized by XPS and TEM analysis (Fig. S9–S12†). NiO_x and CoO_x components were confirmed *via* the mixed valence states and metallic oxides, respectively.

3.3 Photocatalytic O_2-evolution performance

Photocatalytic performances of CN-*x*NiCoO and NiCoO were evaluated by the photocatalytic O_2 evolution reaction by using $AgNO_3$ as the electron scavenger. O_2 was not detected in the photocatalytic O_2 evolution measurement for NiCoO under the same conditions, thus indicating that NiCoO did not work as a photocatalyst. As shown in Fig. 4a and S13a,† under full-arc irradiation, photocatalytic O_2 production activities of CN-*x*NiCoO gradually increased with increasing the NiCoO amount, and the highest OER rate reached 56.8 μmol h^{-1} for the optimized CN-1.00NiCoO sample, which was almost 4.6 times that of bare CN-0.00NiCoO (12.4 μmol h^{-1}) (initial reaction rates were adopted because the metallic Ag^0 reduced by Ag^+ would be

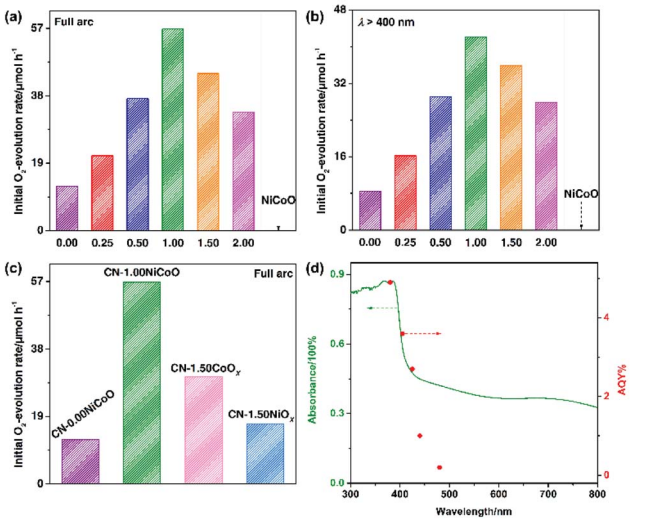

Fig. 4 Photocatalytic O_2-evolution rates of CN-*x*NiCoO (x = 0.00, 0.25, 0.50, 1.00, 1.50 and 2.00) and NiCoO under (a) full-arc and (b) under visible-light irradiation (λ > 400 nm); (c) photocatalytic O_2-evolution rates of CN-0.00NiCoO, CN-1.00NiCoO, CN-1.50NiO_x and CN-1.50CoO_x under full-arc irradiation; (d) wavelength-determined AQYs for CN-1.00NiCoO at different wavelengths. Measurement conditions: 50 mg photocatalyst and 160 mg La_2O_3 were dispersed in 80 mL $AgNO_3$ (0.01 M) aqueous solution.

gradually deposited on the surface of photocatalysts to hinder the light absorption and cover the reactive sites with the reaction time prolonging (Fig. S14†)). When further increasing the NiCoO amount, the photocatalytic O_2-evolution activity of CN-*x*NiCoO decreased since excessive NiCoO blocked the light absorption for CN. Photocatalytic O_2-evolution activities of CN-*x*NiCoO under visible-light irradiation ($\lambda > 400$ nm) are shown in Fig. 4b, and the highest O_2 production rate of the optimized CN-1.00NiCoO (42.0 μmol h^{-1}) was 5 times that of bare CN-0.00NiCoO (8.4 μmol h^{-1}). Furthermore, Fig. 4d shows AQYs of CN-1.00NiCoO for O_2 production at different wavelengths, and the AQY achieved 4.9% at 380 nm (the time courses of photocatalytic O_2 evolution under different wavelengths (380, 405, 425, 440 and 480 nm) over CN-1.00NiCoO are presented in Fig. S15†). The good consistency between the AQY values at different wavelengths and the optical absorption edge indicated that the O_2 evolution reaction was definitely induced by the photo-excitation of CN. Moreover, Fig. S16† shows the XPS results of CN-1.00NiCoO and CN-1.00NiCoO-R obtained by recycling the photocatalysts after the photocatalytic O_2 evolution reaction. There was little difference for the chemical states of Ni and Co before and after the photocatalytic O_2 evolution reaction. In addition, it is noteworthy that the OER rate of CN-1.00NiCoO had the highest value compared with other CN-based materials (Fig. 4c and S13b†). CN-1.50NiO_x and CN-1.50CoO_x demonstrated improved photocatalytic O_2-evolution activities (16.8 and 30.2 μmol h^{-1}, respectively) under full-arc irradiation compared with CN-0.00NiCoO but much lower than that of CN-1.00NiCoO. Furthermore, Table S1† presents the comparison of the photocatalytic O_2-evolution performance of CN-1.00NiCoO and some other reported cocatalyst modified CN, and NiCoO coupled CN took the leading position. These photocatalytic O_2 evolution results indicated that coupling NiCoO with CN can greatly facilitate the oxidation reaction from water, and NiCoO exhibited a superior OER cocatalytic effect to other cocatalysts.

3.4 Optical properties and photo-generated charge carrier dynamics

As shown in Fig. S17,† bare NiCoO presented a flat plot throughout the UV-vis range with a high absorption coefficient, and all the hybrid $NiCo_2O_4$/g-C_3N_4 photocatalysts showed slightly red shifts of absorption edges and increased absorption intensities in the region of 450–800 nm compared with CN-0.00NiCoO. The enhanced optical absorption properties could be ascribed to the coupled structure of NiCoO and CN, in which surface bonding states were built. Moreover, to further investigate the superior cocatalytic effect of NiCoO for CN, PL and (photo)electrochemical measurements for CN-0.00NiCoO, CN-1.00NiCoO, CN-1.50NiO_x and CN-1.50CoO_x were carried out to investigate the efficiency for charge transfer. Fig. 5a presents the PL spectra of the above samples. All the samples showed an emission wavelength at around 440 nm, and CN-1.00NiCoO showed the weakest intensity as compared to those of CN-0.00NiCoO, as well as NiO_x and CoO_x coupled CN, demonstrating the efficient promotion of the rapid photo-generated

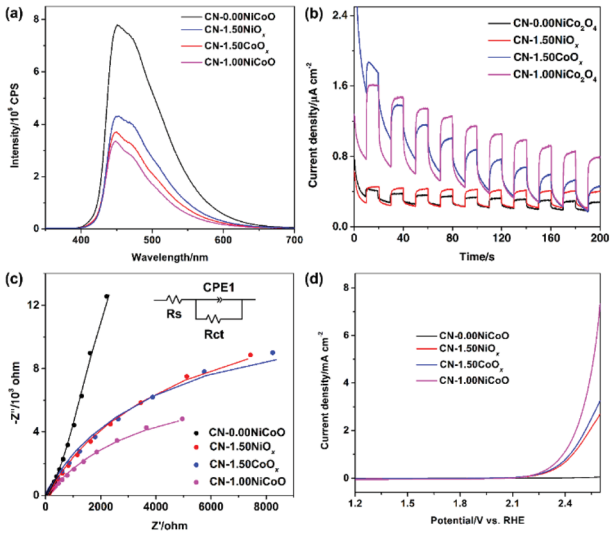

Fig. 5 (a) PL, (b) transient photocurrent density (full-arc irradiation, applied voltage of +0.6 V *vs.* Ag/AgCl), (c) EIS (applied voltage of +1.0 V *vs.* Ag/AgCl) and (d) LSV curves of CN-0.00NiCoO, CN-1.50NiO_x, CN-1.50CoO_x and CN-1.00NiCoO. Electrolyte: 0.5 M Na_2SO_4.

charge carrier transfer between CN and NiCoO. In addition, Fig. 5b shows that CN-1.00NiCoO has the highest photocurrent density, indicating that the separation and migration of photo-generated hole–electron pairs for CN under light irradiation were greatly promoted by the coupling of NiCoO. Fig. 5c presents the EIS plots of the electrodes. The CN-1.00NiCoO electrode showed an obviously smaller arc radius than those of the others, indicating lower charge-transfer impedance as well as easier charge exchange between the electrode and electrolyte.[40] Fig. 5d presents the LSV curves of CN-0.00NiCoO, CN-1.50NiO_x, CN-1.50CoO_x and CN-1.00NiCoO samples for the OER. An improved onset potential for the anodic current and enhanced current density were achieved for CN-1.00NiCoO as compared to those of the others. The above results proved that the coupling NiCoO with CN can greatly facilitate the oxidation reaction from water. In addition, the *C–V* results indicated the good chemical stability of the $NiCo_2O_4$/g-C_3N_4 composite (Fig. S18†).

3.5 Photocatalytic overall water splitting

According to the reports, overall water splitting reaction can be performed on CN through loading appropriate cocatalysts, and dual cocatalysts including HER and OER cocatalysts assembled on CN can lead to efficient goal-oriented migration of photo-generated electron–hole pairs, thereby improving the interfacial separation of photo-generated charge carriers and accelerating water splitting reaction kinetics for enhanced photocatalytic activity.[48–53] As a consequence, the Pt–CN–NiCoO photocatalyst was constructed to perform overall water splitting, in which Pt and NiCoO were employed as efficient HER and OER cocatalysts for CN, respectively. Fig. S19a and b† show that the structures of CN-0.00NiCoO, CN-3Pt and 3Pt-CN-1.00NiCoO were consistent with the typical XRD and FTIR characteristics of g-C_3N_4, respectively. Furthermore, according

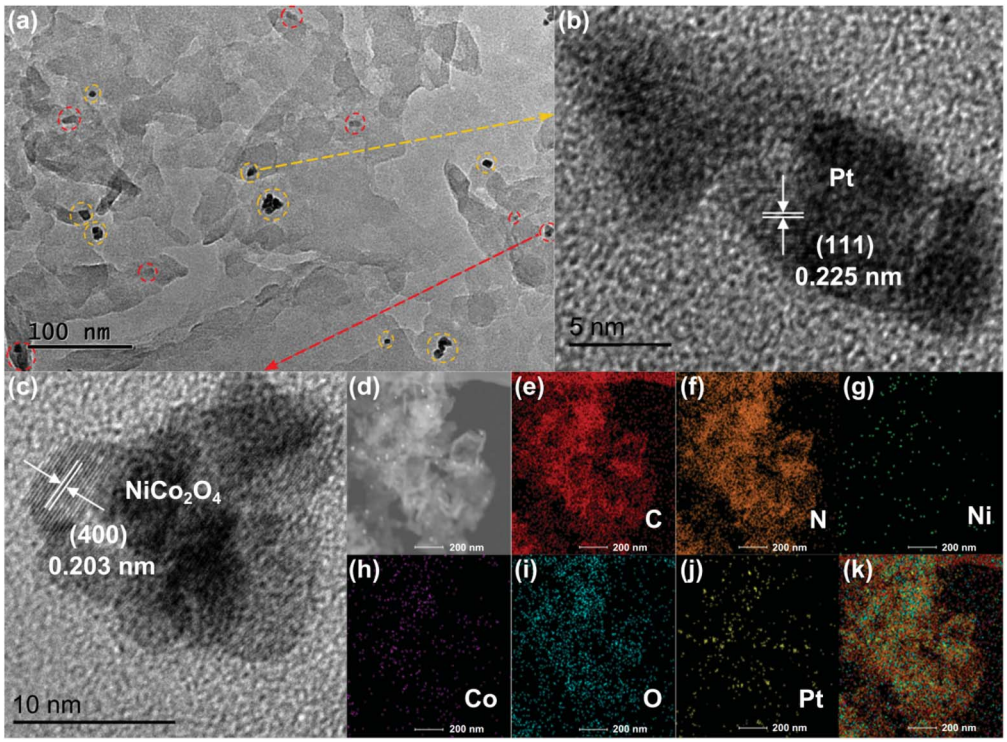

Fig. 6 (a) TEM image, (b and c) HRTEM images, (d) STEM image and (e–j) EDX elemental mapping results of (e) C, (f) N, (g) Ni, (h) Co, (i) O, (j) Pt elements and (k) their overlapping for 3Pt-CN-1.00NiCoO. Red and yellow circles in (a) demonstrated NiCoO and Pt, respectively.

to the XPS (Fig. S20†), TEM (Fig. 6a), HRTEM (Fig. 6b and c), STEM (Fig. 6d) and corresponding EDX elemental mapping of 3Pt-CN-1.00NiCoO (Fig. 6e–k), it is demonstrated that Pt small nanoparticles and NiCoO are decorated on the CN nanosheets with spatially separated positions. 3Pt-CN-1.00NiCoO had quite similar light absorption to CN-1.00NiCoO (Fig. S21†). Fig. S22† shows that 3Pt-CN-1.00NiCoO displayed the weakest PL intensity, indicating the great improvement of photo-generated charge carrier transfer ability. Fig. 7a and S23† show the polarization curves of CN-0.00NiCoO and 3Pt-CN-1.00NiCoO for overall water splitting. Significantly, 3Pt-CN-1.00NiCoO manifested obviously improved onset potentials for both HER and OER, as well as enhanced cathode and anode current densities, demonstrating that dual Pt and NiCoO cocatalysts could accelerate the water reduction and oxidation selectively for CN. As expected, 3Pt-CN-1.00NiCoO showed photocatalytic overall water splitting performance with simultaneous evolution of H_2 and O_2 in a stoichiometric ratio of around 2 : 1 under full-arc (21.7 and 10.6 μmol h^{-1}) and visible-light (7.4 and 3.6 μmol h^{-1}) irradiation (Fig. 7b, c and S24†). Meanwhile, the AQY of 3Pt-CN-1.00NiCoO for H_2 evolution was about 2.8% at 380 nm. For the overall water splitting reaction, the total amount of O_2 evolved in 36 h was 395.4 μmol, which was much larger than the lattice oxygen of $NiCo_2O_4$ in 3Pt-CN-1.00NiCoO (8.3 μmol for oxygen atoms). What's more, the turnover number (TON) was far greater than unity (>1). As a result, it was proved that the evolved O_2 came from water *via* the photocatalyst-based photocatalytic reaction. Besides, CN co-loaded with Pt and NiCoO displayed enhanced activity compared with which loaded with either Pt or NiCoO, and the Pt–NiCoO couple could display a superior cocatalytic effect compared to Pt–NiO_x and Pt–CoO_x couples in the promotion of photocatalytic overall water splitting reaction (Fig. 7d). Table S2† lists the rates and AQYs of photocatalytic overall water splitting over g-C_3N_4 modified with a series of cocatalysts in recent years, and Pt–NiCoO couple assisted g-C_3N_4 in this work showed excellent photocatalytic overall water splitting activity as compared to most of the other cocatalyst assisted g-C_3N_4 photocatalysts. Moreover, the cyclic test of 3Pt-CN-1.00NiCoO for overall water splitting under full-arc irradiation exhibited no decay in 39 h for three cyclic tests, and the amounts of H_2 and O_2 did not decrease in the dark when light was turned off for 3 h in the first cycle (Fig. 7b). Fig. S20† presents the XRD patterns and XPS results of 3Pt-CN-1.00NiCoO and 3Pt-CN-1.00NiCoO-R obtained by recycling the photocatalyst after photocatalytic overall water splitting reaction. Little difference was observed for the photocatalyst before and after the photocatalytic reaction. These results indicated that the Pt–NiCoO dual cocatalyst loaded CN-based system had good photocatalytic stability. In Fig. S25,† the TEM and STEM images of 3Pt-CN-1.00NiCoO-R show that cocatalysts were clearly anchored on the CN nanosheets after reaction, and the notable deviation in elemental scope and the scattered distribution for EDX elemental mapping images further indicated that Pt small nanoparticles and NiCoO are decorated on the CN nanosheets with spatially separated positions. From the XRD and XPS results it was detected that Pt and NiCoO were obviously present in both 3Pt-CN-1.00NiCoO and 3Pt-CN-

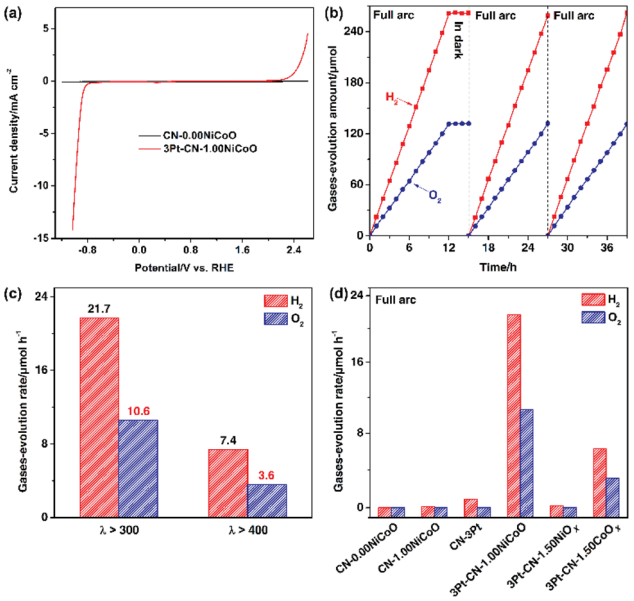

Fig. 7 (a) LSV curves of CN-0.00NiCoO and 3Pt-CN-1.00NiCoO (electrolyte: 0.5 M Na_2SO_4); (b) time courses of H_2 and O_2 production for photocatalytic overall water splitting under full-arc irradiation over 3Pt-CN-1.00NiCoO; (c) photocatalytic activities for overall water splitting on 3Pt-CN-1.00NiCoO under full-arc and visible-light irradiation ($\lambda > 400$ nm); (d) photocatalytic performance of overall water splitting on CN-0.00NiCoO, CN-1.00NiCoO, CN-3Pt, 3Pt-CN-1.00NiCoO, 3Pt-CN-1.50NiO_x and 3Pt-CN-1.50CoO_x under full-arc irradiation. Photocatalytic reaction measurement conditions: 50 mg photocatalyst dispersed in 80 mL deionized water without any sacrificial reagent.

1.00NiCoO-R (Fig. S20†), which indicated that Pt and NiCoO cocatalysts were not lost after reaction.

3.6 Photocatalytic mechanism

According to the above results, as shown in Fig. S26,† when NiCoO was employed as an efficient OER cocatalyst, the cooperative effect between NiCoO and CN could reduce the overpotential of the OER from water and promote the transfer of photo-generated charge carriers. When Pt (HER cocatalyst) was integrated with $NiCo_2O_4$/g-C_3N_4, overall water splitting was successfully achieved for CN. In the reaction process, electrons were generated in the conduction band (CB) while holes in the valence band (VB) of CN under light irradiation. Afterwards, the electrons in the CB of CN promptly transported to Pt for water reduction to produce H_2. The holes in the VB of CN transported to NiCoO for water oxidation to generate O_2. Due to the superior dual cocatalytic effect, (Pt, $NiCo_2O_4$)/g-C_3N_4 exhibited enhanced photocatalytic overall water splitting activity as compared to some other dual cocatalyst loaded CN.

4. Conclusions

2D/2D coupled CN-*x*NiCoO photocatalysts were fabricated *via* an *in situ* growth strategy. NiCoO worked as a novel OER cocatalyst and the assembly of NiCoO onto CN led to a reduced overpotential for oxidation reaction from water and promoted photo-generated charge carrier transfer, resulting in enhanced photocatalytic O_2 evolution for the $NiCo_2O_4$/g-C_3N_4 photocatalyst. In addition, Pt was integrated with $NiCo_2O_4$/g-C_3N_4, and the derived (Pt, $NiCo_2O_4$)/g-C_3N_4 photocatalyst showed overall water splitting into H_2 and O_2 in a stoichiometric ratio of 2 : 1. Briefly, this work demonstrates a reliable strategy for CN to develop a photocatalytic overall water splitting system *via* assistance with high-efficiency dual reduction and oxidation cocatalysts.

Author contributions

Cheng Cheng and Liuhao Mao: investigation, formal analysis, and writing-original draft preparation. Fei Xue, Shichao Zong and Botong Zheng: writing-review & editing. Jinwen Shi and Liejin Guo: supervision, project administration, resources and formal analysis.

Conflicts of interest

There are no conflicts to declare.

Acknowledgements

This work is supported by the Basic Science Center Program for Ordered Energy Conversion of the National Natural Science Foundation of China (No. 51888103).

Notes and references

1 Z. Wang, C. Li and K. Domen, *Chem. Soc. Rev.*, 2019, **48**, 2109–2125.
2 Q. Wang and K. Domen, *Chem. Rev.*, 2019, **120**, 919–985.
3 W. Ding, J. Shi, W. Wei, C. Cao and H. Jin, *Int. J. Hydrogen Energy*, 2021, **46**, 2899–2904.
4 T. Takata, J. Jiang, Y. Sakata, M. Nakabayashi, N. Shibata, V. Nandal, K. Seki, T. Hisatomi and K. Domen, *Nature*, 2020, **581**, 411–414.
5 K. Watanabe, A. Iwase and A. Kudo, *Chem. Sci.*, 2020, **11**, 2330–2334.
6 X. Chen and S. S. Mao, *Chem. Rev.*, 2007, **107**, 2891–2959.
7 J. Liu, Y. Li, X. Zhou, H. Jiang, H. Yang and C. Li, *J. Mater. Chem. A*, 2020, **8**, 17–26.
8 M. W. Kanan and D. G. Nocera, *Science*, 2008, **321**, 1072–1075.
9 Z. Yi, J. Ye, N. Kikugawa, T. Kako, S. Ouyang, H. S. Williams, H. Yang, J. Cao, W. Luo, Z. Li, Y. Liu and R. L. Withers, *Nat. Mater.*, 2010, **9**, 559–564.
10 Z. Chen, T. Jaramillo, T. Deutsch, A. Kleiman-Shwarsctein, A. Forman, N. Gaillard, R. Garland, K. Takanabe, C. Heske, M. Sunkara, E. McFarland, K. Domen, E. Miller, J. Turner and H. Dinh, *J. Mater. Res.*, 2010, **25**, 3–16.
11 P. A. Hernley, S. A. Chavez, J. P. Quinn and S. Linic, *ACS Photonics*, 2017, **4**, 979–985.
12 J. Yang, D. Wang, H. Han and C. Li, *Acc. Chem. Res.*, 2013, **46**, 1900–1909.

13 Q. Yue, Y. Wan, Z. Sun, X. Wu, Y. Yuan and P. Du, *J. Mater. Chem. A*, 2015, **3**, 16941–16947.
14 J. Ran, J. Zhang, J. Yu, M. Jaroniec and S. Qiao, *Chem. Soc. Rev.*, 2014, **43**, 7787–7812.
15 Y. Zhang, J. Shi, Z. Huang, X. Guan, S. Zong, C. Cheng, B. Zheng and L. Guo, *Chem. Eng. J.*, 2020, **401**, 126135.
16 W. Wang, T. An, G. Li, D. Xia, H. Zhao, J. Yu and P. Wong, *Appl. Catal., B*, 2017, **217**, 570–580.
17 S. Yi, J. Yan, B. Wulan, S. Li, K. Liu and Q. Jiang, *Appl. Catal., B*, 2017, **200**, 477–483.
18 H. Cheng, X. Lv, S. Cao, Z. Zhao, Y. Chen and W. Fu, *Sci. Rep.*, 2016, **6**, 19846–19855.
19 X. Yue, S. Yi, R. Wang, Z. Zhang and S. Qiu, *Nanoscale*, 2016, **8**, 17516–17523.
20 J. Tang, D. Yang, W. Zhou, R. Guo, W. Pan and C. Huang, *J. Catal.*, 2019, **370**, 79–87.
21 L. Bi, X. Gao, L. Zhang, D. Wang, X. Zou and T. Xie, *ChemSusChem*, 2018, **11**, 276–284.
22 Z. Wang, Z. Qi, X. Fan, D. Leung, J. Long, Z. Zhang, T. Miao, S. Meng, S. Chen and X. Fu, *Appl. Catal., B*, 2021, **281**, 119443–119453.
23 Z. Qin, Y. Chen, Z. Huang, J. Su and L. Guo, *J. Mater. Chem. A*, 2017, **5**, 19025–19035.
24 J. Yang, C. Yu, S. Liang, S. Li, H. Huang, X. Han, C. Zhao, X. Song, C. Hao, P. M. Ajayan and J. Qiu, *Chem. Mater.*, 2016, **28**, 5855–5863.
25 X. Yan, K. Li, L. Lyu, F. Song, J. He, D. Niu, L. Liu, X. Hu and X. Chen, *ACS Appl. Mater. Interfaces*, 2016, **8**, 3208–3214.
26 X. Wang, K. Maeda, A. Thomas, K. Takanabe, G. Xin, J. M. Carlsson, K. Domen and M. Antonietti, *Nat. Mater.*, 2008, **8**, 76–80.
27 W. Ong, L. Tan, Y. H. Ng, S. Yong and S. Chai, *Chem. Rev.*, 2016, **116**, 7159–7329.
28 Z. Zhou, Y. Zhang, Y. Shen, S. Liu and Y. Zhang, *Chem. Soc. Rev.*, 2018, **47**, 2298–2321.
29 B. Yan, Z. Chen and Y. Xu, *Chem.–Asian J.*, 2020, **15**, 2329–2340.
30 J. Liu, Y. Liu, N. Liu, Y. Han, X. Zhang, H. Huang, Y. Lifshitz, S. T. Lee, J. Zhong and Z. Kang, *Science*, 2015, **347**, 970–974.
31 C. Cheng, J. Shi, F. Du, S. Zong, X. Guan, Y. Zhang, M. Liu and L. Guo, *Catal. Sci. Technol.*, 2019, **9**, 7016–7022.
32 C. Cheng, J. Shi, Y. Hu and L. Guo, *Nanotechnology*, 2017, **28**, 164002–164010.
33 H. Che, G. Che, P. Zhou, C. Liu, H. Dong, C. Li, N. Song and C. Li, *Chem. Eng. J.*, 2020, **382**, 122870–122878.
34 H. Yu, R. Shi, Y. Zhao, T. Bian, Y. Zhao, C. Zhou, G. I. Waterhouse, L. Wu, C. Tung and T. Zhang, *Adv. Mater.*, 2017, **29**, 1605148–1605154.
35 Y. Zhang, J. Liu, G. Wu and W. Chen, *Nanoscale*, 2012, **4**, 5300–5303.
36 D. Zhang, Y. Guo and Z. Zhao, *Appl. Catal., B*, 2018, **226**, 1–9.
37 T. Song, P. Zhang, T. Wang, A. Ali and H. Zeng, *Appl. Surf. Sci.*, 2019, **464**, 195–204.
38 G. Liu, G. Zhao, W. Zhou, Y. Liu, H. Pang, H. Zhang, D. Hao, X. Meng, P. Li, T. Kako and J. Ye, *Adv. Funct. Mater.*, 2016, **26**, 6822–6829.
39 F. Xue, M. Liu, C. Cheng, J. Deng and J. Shi, *ChemCatChem*, 2018, **10**, 5441–5448.
40 Y. Zhang, Z. Huang, J. Shi, X. Guan, C. Cheng, S. Zong, Y. Huangfu, L. Ma and L. Guo, *Appl. Catal., B*, 2020, **272**, 119009.
41 Y. Zhang, Z. Chen, J. Li, Z. Lu and X. Wang, *J. Energy Chem.*, 2021, **54**, 36–44.
42 Y. Li, P. Hasin and Y. Wu, *Adv. Mater.*, 2010, **22**, 1926–1929.
43 F. Xue, Y. Si, M. Wang, M. Liu and L. Guo, *Nano Energy*, 2019, **62**, 823–831.
44 C. Cheng, S. Zong, J. Shi, F. Xue, Y. Zhang, X. Guan, B. Zheng, J. Deng and L. Guo, *Appl. Catal., B*, 2020, **265**, 118620–118628.
45 C. Li, Y. Du, D. Wang, S. Yin, W. Tu, Z. Chen, M. Kraft, G. Chen and R. Xu, *Adv. Funct. Mater.*, 2017, **27**, 1604328–1604335.
46 B. Luo, R. Song, J. Geng, X. Liu, D. Jing, M. Wang and C. Cheng, *Appl. Catal., B*, 2019, **256**, 117819–117828.
47 Y. Zhang, J. Shi, C. Cheng, S. Zong, J. Geng, X. Guan and L. Guo, *Appl. Catal., B*, 2018, **232**, 268–274.
48 Z. Pan, Y. Zheng, F. Guo, P. Niu and X. Wang, *ChemSusChem*, 2017, **10**, 87–90.
49 S. Sun, Y. Zhang, G. Shen, Y. Wang, X. Liu, Z. Duan, L. Pan, X. Zhang and J. Zou, *Appl. Catal., B*, 2019, **243**, 253–261.
50 L. Lin, Z. Lin, J. Zhang, X. Cai, W. Lin, Z. Yu and X. Wang, *Nat. Catal.*, 2020, **3**, 649–655.
51 G. Zhang, Z. Lan, L. Lin, S. Lin and X. Wang, *Chem. Sci.*, 2016, **7**, 3062.
52 Y. Li, S. Zhu, X. Kong, Y. Liang, Z. Li, S. Wu, C. Chang, S. Luo and Z. Cui, *J. Colloid Interface Sci.*, 2021, **586**, 778–784.
53 L. Chen, X. Zhao, X. Duan, J. Zhang, Z. Ao, P. Li, S. Wang, Y. Wang, S. Cheng, H. Zhao, F. He, P. Dong, C. Zhao, S. Wang and H. Sun, *ACS Sustainable Chem. Eng.*, 2020, **8**, 14386–14396.

